nature geoscience

Analysis

https://doi.org/10.1038/s41561-026-02070-6

Planetary energy budget during abrupt glacial climate events set by Atlantic Ocean heat valve

Received: 3 September 2025

Accepted: 14 July 2026

Published online: 10 August 2026

Check for updates

Christo Buizert[1] ✉, Ayako Abe-Ouchi[2], Guido Vettoretti[3], Xu Zhang[4,5], Yuta Kuniyoshi[2], Sarah Shackleton[6], Sune Olander Rasmussen[2], Joel B. Pedro[7,8], Eric D. Galbraith[9,10,11] & Thomas F. Stocker[12]

During Pleistocene ice ages, abrupt climate changes co-occurred with switches in Atlantic Meridional Overturning Circulation (AMOC) strength. The global impact and characteristic north–south temperature pattern of these events is typically explained via interhemispheric redistribution of heat in a conceptual framework called the 'thermal bipolar seesaw'. Here we synthesize recent work on an emerging alternative framework centred instead on the global ocean heat content and planetary energy budget, which we illustrate using simulations of spontaneous abrupt climate change in three climate models. The strong and weak AMOC modes are associated with oceanic and planetary heat loss and heat gain, respectively, facilitated via changes to North Atlantic deep convection and radiative feedbacks that set the top-of-the-atmosphere energy budget. Antarctic and Greenland temperatures, as recorded in ice cores, reflect ocean heat content and the rate of North Atlantic heat loss, respectively. Climate instability at intermediate glacial states reflects an inability to balance global ocean heat uptake with North Atlantic heat loss for either of the two AMOC modes. Our synthesis suggests that the AMOC strength acts as a 'heat valve' that alters planetary temperature by changing the radiative balance. This implies amplified planetary heat uptake in response to projected future AMOC weakening.

The Dansgaard–Oeschger (DO) cycle is a sequence of alternating cold (stadial) and warm (interstadial) stages recorded in Greenland ice cores[1]. Evidence from marine sediments and climate modelling have linked the DO cycle to abrupt Atlantic Meridional Overturning Circulation (AMOC) variations, with the Greenland cold and warm stages corresponding to a weak and strong AMOC, respectively[2–4]. Recent models suggest the DO cycle is a spontaneous self-sustained oscillation of the coupled ocean–atmosphere–sea-ice system[5–11]. The deepwater formation that sustains the AMOC is enabled through the northward transport of salinity and through (wintertime) open ocean heat loss—conditions that are promoted by a strong AMOC. Salt advection and sea ice dynamics are thus fast-acting positive feedbacks[11,12] that can account for convection bistability[13] and the abruptness of AMOC transitions during the DO cycle. During the weak AMOC phase, extended sea-ice cover and upper ocean stratification by cold freshwater reduce heat loss to the atmosphere and suppress deep convection[14]. Gradual subsurface warming then slowly erodes this stratification until the sudden resumption of deep convection and associated release of heat stored in the subsurface melts back the sea ice and resumes the AMOC[6,15–17]. In this way, a slow-acting negative feedback (or restoring force) is provided by deep-ocean temperatures[16,17], and possibly Southern Ocean processes[18].

Antarctic ice core records show gradual warming during Greenland stadials and gradual cooling during interstadials[19,20], such that

A full list of affiliations appears at the end of the paper. ✉e-mail: christo.buizert@oregonstate.edu

https://doi.org/10.1038/s41561-026-02070-6

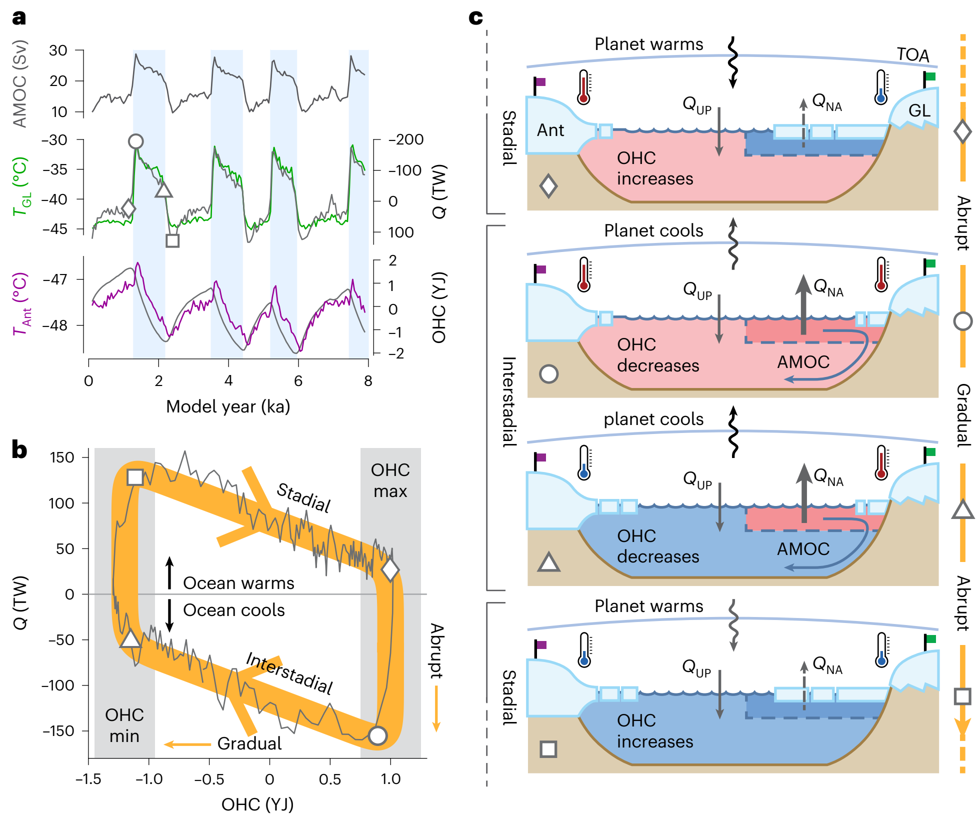

Fig. 1 | Conceptual framework of the global DO–OHC cycle. **a**, Simulated Greenland (T_{GL}) and Antarctic (T_{Ant}) temperatures (green and purple, respectively, left axes) overlaid on simulated global surface heat flux Q (sum of radiative, sensible and latent heat fluxes; note reverse scale; TW = 10^{12} W, right axis) and OHC (YJ = 10^{24} J, right axis). Vertical blue shading indicates interstadial (strong AMOC) conditions. Model year is given in thousands of years (ka). **b**, OHC vs global-mean ocean surface heat flux Q for the DO–OHC cycle: idealized (orange) and model simulation (grey line, 30-year running mean). **c**, Idealized cartoon of four time slices in the DO–OHC cycle, with symbols (◇, ○, △ and □) linking them to panels **a** and **b**. The figure depicts an idealized ocean cross section with the North Atlantic on the right and the Antarctic (Ant) and Greenland (GL) ice sheets on the left and right, respectively. Q_{NA} gives the North Atlantic surface heat flux and Q_{UP} the heat uptake in the remainder of the ocean, such that $Q = Q_{NA} + Q_{UP}$. In our sign convention positive and negative Q values warm and cool the ocean, respectively. Arrows denote the physical direction of heat transport (rather than sign convention). The net planetary energy balance is shown with the wavy arrow at the TOA.

Greenland temperature is strongly anti-correlated with the time derivative of the Antarctic temperature. The thermal bipolar seesaw model[21,22] explains this coupling as an interhemispheric redistribution of heat via perturbations to the northward cross-equatorial heat transport by the AMOC; this results in opposite North and South Atlantic sea surface temperature (SST) anomalies, with Antarctic temperature reflecting the latter buffered by the Southern Ocean heat reservoir[22].

Important developments since the establishment of the thermal bipolar seesaw framework include: the ability of climate models to simulate freshwater-forced[23–25], and more recently spontaneous or self-sustained[5–11], DO events; detailed, well-dated records of mean ocean temperature[26,27]; observed and modelled constraints on the planetary energy balance during AMOC variations[23,28]; a recognition of the critical role of sea ice and its feedbacks[12,15,29]; observational[30,31] and conceptual[24] advances recognizing the role of the global ocean interior temperature; and mid-latitude glacier lengths that vary synchronously, rather than oppositely, between the hemispheres[32]. These advances, found across various published works, prompt a reevaluation of the global energetics of past abrupt AMOC variability. Our aim here is to synthesize these ideas into a coherent framework that places global ocean heat content (OHC) at its centre. We refer to these globally connected cycles as DO–OHC oscillations. We assess the framework using simulations of spontaneous, self-sustained DO–OHC oscillations in three atmosphere–ocean coupled models: CCSM4[5], MIROC4m[6] and COSMOS[7] (Methods). All three models simulate realistic DO cycles in Greenland temperature, and two of them simulate realistic millennial-scale temperature cycles in Antarctica (Extended Data Fig. 1).

An updated framework for global climate coupling during the DO–OHC cycle

To introduce the framework, we step through a single DO–OHC cycle (Fig. 1), starting at the end of the weak AMOC phase (time ◇) when the North Atlantic is still covered in extensive sea ice. Subsequently, the AMOC increases abruptly into its strong phase (time ○), which in the North Atlantic leads to increased SST, reduced (wintertime) sea ice and extensive heat loss to the atmosphere mainly via deep convection (Q_{NA}, positive values of Q warm the ocean in our sign convention). This local heat loss exceeds ocean surface heat uptake Q_{UP} in the remainder of the ocean ($|Q_{NA}| > |Q_{UP}|$), and therefore the net whole-ocean surface heat flux is negative ($Q = Q_{UP} + Q_{NA} < 0$), causing OHC to decrease. Northern high-latitude warming leads to increased outgoing longwave radiation and planetary energy loss at the top of the atmosphere (TOA). This TOA radiative imbalance enables, and is maintained by, continued strong ocean heat loss in the North Atlantic.

OHC continues to decrease for ~1,000 years until the end of the strong AMOC phase (time Δ), at which point the global ocean has reached the lowest heat content in the cycle. The AMOC decreases abruptly into its weak phase (time □) with low North Atlantic SST and extensive (wintertime) sea ice. With the cessation of deep convection, North Atlantic heat loss is now smaller than heat uptake in the rest of the ocean ($|Q_{NA}| < |Q_{UP}|$), causing OHC to increase. The TOA radiative

https://doi.org/10.1038/s41561-026-02070-6

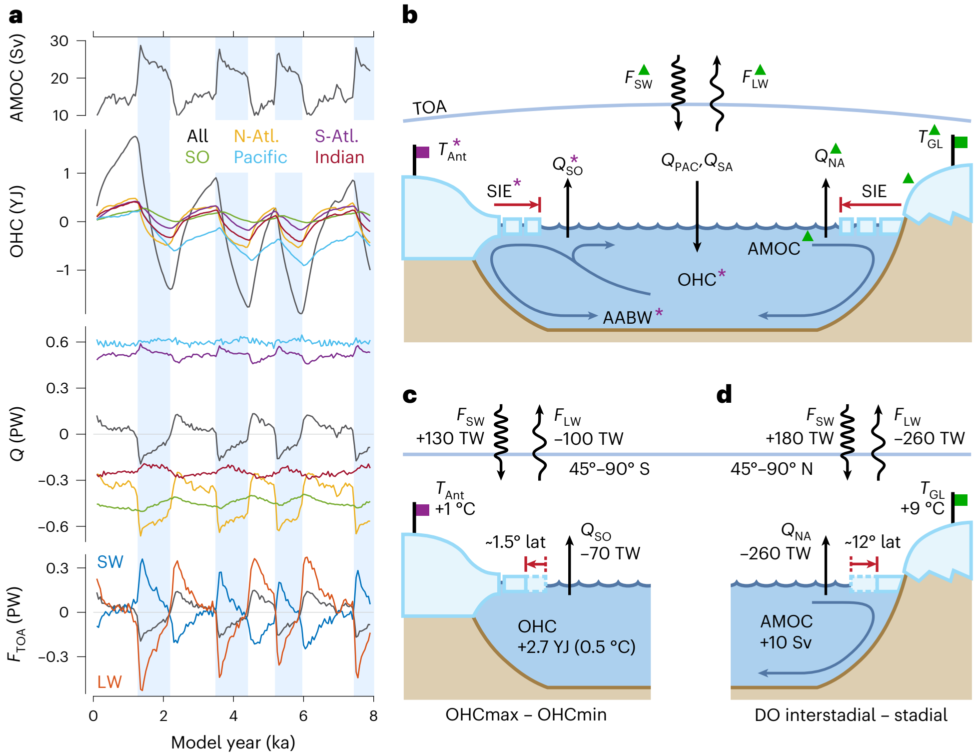

Fig. 2 | The global DO–OHC cycle in climate models. a, Time series of CCSM4 spontaneous DO–OHC oscillations; Extended Data Fig. 3 shows the other models. From top to bottom: AMOC strength (Sv = $10^6\,m^3\,s^{-1}$); OHC of individual ocean basins (colour coded as listed, YJ = 10^{24} J; N-Atl and S-Atl are the North and South Atlantic, respectively); total ocean surface heat flux of individual ocean basins (positive means ocean heat uptake, same colour coding as OHC plot, PW = 10^{15} W); TOA total (grey), net longwave (orange) and net shortwave (blue) radiative flux anomalies (positive means Earth system heat uptake). Vertical blue shading indicates interstadial (strong AMOC) conditions. **b**, Idealized ocean cross section with variables of interest: TOA net incoming shortwave (F_{SW}) and net outgoing longwave (F_{LW}); ocean surface heat fluxes in Southern (Q_{SO}), Pacific (Q_{PAC}), South Atlantic (Q_{SA}) and North Atlantic (Q_{NA}) oceans; sea ice extent (SIE) in the Southern Ocean and North Atlantic; Antarctic (T_{Ant}) and Greenland (T_{GL}) temperatures; OHC; and major overturning circulation. Variables marked with green triangles (anti-) correlate with Q, variables marked with purple asterisks (anti-) correlate with OHC. Arrows indicate physical direction of heat transport. **c**, Simulated anomalies for OHC maximum minus OHC minimum state (TOA flux averaged over 90° S–45° S). Printed anomalies follow sign convention, with negative and positive numbers denoting ocean/planetary cooling and warming, respectively. Approximate changes in sea ice extent (SIE) given in degrees latitude (lat). **d**, As panel **c**, but for DO interstadial minus DO stadial state (TOA flux averaged over 90° N–45° N).

imbalance likewise reverses, causing net planetary energy gain. OHC continues to increase for ~1,000 years until the climate system is back at the end of the weak AMOC phase (time ◇), at which point OHC is at a maximum.

In this framework, AMOC deep convection acts as an 'ocean heat valve': when the valve is open (strong AMOC), energy drains from the ocean and planet; when the valve is closed (weak AMOC), energy is retained and accumulates in the ocean interior. In the remainder of this paper, we will elaborate on the framework and its expression in the models. We organize the paper along four principles that help understand global climate coupling during the DO–OHC cycle:

(1) Globally synchronous variations in OHC are driven by abrupt variations in North Atlantic heat loss associated with convection bistability and AMOC switching during the DO–OHC cycle.
(2) OHC variations are enabled by radiative imbalance at the top of the atmosphere, such that the planetary energy balance mirrors that of the ocean.
(3) Antarctic (T_{Ant}) and Greenland (T_{GL}) temperatures reflect OHC and the rate of ocean heat loss, respectively.
(4) The DO–OHC cycle is a spontaneous self-sustained oscillation under intermediate climate conditions, with timing characteristics that depend on the background climate and CO_2.

Ocean heat content

Global OHC is controlled via the integrated net heat flux Q at the ocean surface. The global ocean takes up heat in the low latitudes, primarily at the East Pacific cold tongue and South Atlantic, and loses heat in the high-latitude Southern, North Pacific and North Atlantic oceans[33,34] (Extended Data Fig. 2).

The simulated North Atlantic surface heat flux Q_{NA} is bimodal and closely linked to the strength of the AMOC (Fig. 2a). The strong and weak overturning modes correspond to high and low rates of ocean heat loss, respectively, reflecting changes to the (wintertime) deep convection in the North Atlantic subpolar gyre[35] (Extended Data Fig. 3b). By contrast, surface heat fluxes in other ocean basins are more stable over time, such that the North Atlantic signal dominates the global net surface heat flux; Q switches between positive (stadial, weak AMOC) and negative (interstadial, strong AMOC) values, resulting in a triangular OHC signal switching between trends of warming and cooling, respectively[16,17,24]. We find that all ocean basins share a similar OHC signal (Fig. 2a). Such triangular, Antarctica-like temperature signals are indeed observed in the deep Atlantic[36]. For basins other than the North Atlantic, the OHC signal is driven by interior ocean heat transfer rather than through their surface heat flux. All three models show increased inter-basin heat export from Indo-Pacific during the strong AMOC phase (Extended Data Fig. 2), with a matching heat import anomaly into the Atlantic where the heat is then lost from the ocean via the surface flux Q_{NA}. The mid-depth ocean dominates the global propagation of OHC anomalies (Supplementary Videos 1–3).

When the simulated climate evolution is plotted in (OHC,Q)-space (Fig. 1b), it makes a clockwise trajectory. Comparing different points along the trajectory illuminates the surface expression of the DO–OHC cycle.

 https://doi.org/10.1038/s41561-026-02070-6

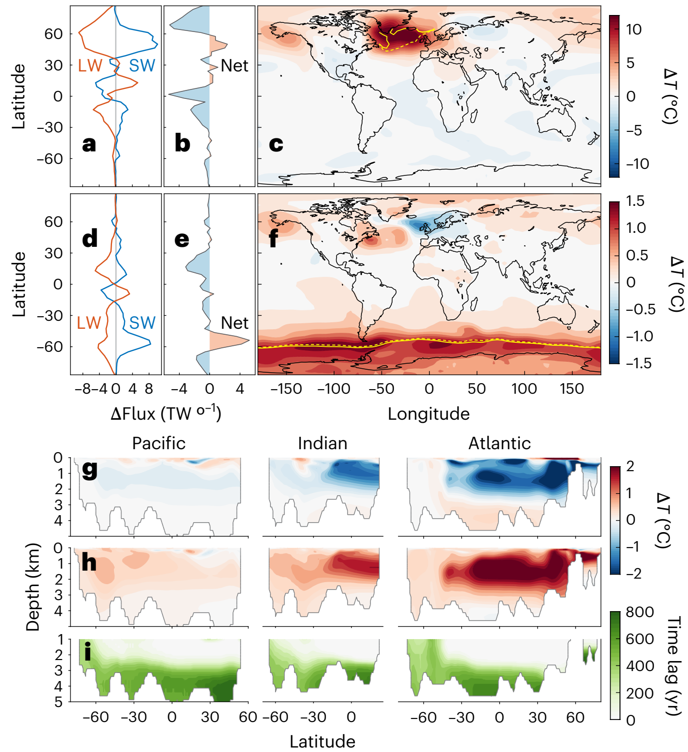

Fig. 3 | Temperature and flux anomalies of the DO–OHC cycle. a–**c**, DO mode anomalies as interstadial minus stadial conditions (Extended Data Fig. 10). **a**, TOA zonal-mean longwave (LW, orange) and shortwave (SW, blue) flux anomalies in units of TW per degree of latitude. **b**, Net radiative TOA flux anomalies. **c**, Surface air temperature anomalies with winter sea ice extent in interstadial (yellow solid line) and stadial (yellow dashed line) conditions. **d**–**f**, As for panels **a**–**c**, but for OHC maximum minus OHC minimum conditions; winter sea ice extent in OHC maximum (yellow solid line) and OHC minimum (yellow dashed line). **g**, Ocean potential temperature anomalies along meridional transects for the DO mode (interstadial minus stadial conditions). **h**, As panel **e** but for the OHC mode (OHC maximum minus OHC minimum conditions). **i**, Time lag that maximizes the Pearson correlation coefficient between local temperature and global-mean ocean temperature. All simulations from the CCSM4 model (210 ppm CO_2); Extended Data Figs. 4 and 5 show the MIROC4m and COSMOS models.

First, evaluating interstadial (strong AMOC) minus stadial (weak AMOC) conditions ('DO mode'), we find the familiar pattern of North Atlantic SST warming[25] and reduced wintertime sea ice extent (Fig. 3c). Viewing this difference along ocean cross sections shows North Atlantic DO warming to be confined to the surface layer, with cooling in the subsurface as seen in prior studies[6,15,24] (Fig. 3g). Second, evaluating the OHC maximum minus the OHC minimum conditions ('OHC mode'), we find that the surface expression of the OHC signal is confined mainly to the Southern Ocean where intermediate and deep waters upwell (Fig. 3f). In the ocean cross sections, we see the OHC signal extend to all ocean basins and depths, with the largest magnitudes in the mid-depth Atlantic (Fig. 3h). Last, we perform a lagged-correlation analysis of ocean temperatures with the global-mean OHC signal (Fig. 3i), which shows the largest lags in the abyssal North Pacific of close to 1,000 years—consequently, for common DO return times of 1,500 years, the deep ocean does not reach equilibrium.

Planetary energy balance

Because our models disregard ice volume changes that could store latent heat[28], the ocean is the dominant planetary heat capacity on the timescale of interest. The TOA planetary radiative energy budget must therefore closely match the ocean heat budget[23]. The TOA and ocean surface heat flux anomalies are closely tied, and neither could exist without the other. Across the DO–OHC cycle, global-mean TOA shortwave (F_{SW}) and longwave (F_{LW}) flux anomalies oppose each other with the latter being larger in magnitude and their sum matching Q (Fig. 2a). The global TOA radiative flux anomaly is positive (planetary heat gain) during the weak AMOC phase and negative (planetary heat loss) during the strong AMOC phase.

North Atlantic surface warming associated with the DO mode drives a negative F_{LW} anomaly (heat loss to space) in the Northern Hemisphere high latitudes, whereas loss of sea ice and continental snow cover drives a positive F_{SW} anomaly via the ice-albedo feedback (Fig. 3a–c). A northward shift in the intertropical convergence zone leads to opposing F_{LW} and F_{SW} anomalies in the northern and Southern Hemisphere tropics, as examined in detail elsewhere[37]. In all three models, TOA planetary heat loss during interstadials (strong AMOC) is broadly distributed between the northern high latitudes and southern tropics (Fig. 3b and Extended Data Figs. 4b and 5b), reflecting global radiative feedbacks that include a southward cross-equatorial atmospheric heat flux anomaly linked to the northward shift in the intertropical convergence zone[37,38]. Zonal-mean flux anomalies associated with the OHC mode show similar patterns of shortwave and longwave anomalies mirrored in the Southern Hemisphere high latitudes[24], though with a planetary net flux anomaly close to zero (Fig. 3d–f).

Bipolar ice core coupling

Polar ice cores historically have had an outsized importance in the study of global DO climate coupling due to their high resolution and precise age control[19]. Greenland and Antarctic ice cores happen to be excellent recorders of the DO and OHC modes, respectively, as they are located in proximity to these modes' respective surface expressions (Fig. 3c,f). Across a DO warming transition, rapid sea-ice loss and SST increase in the North Atlantic drive atmospheric and Greenland warming via the heat flux Q_{NA}, with added warming from enhanced absorption of shortwave radiation locally via the ice-albedo feedback (Fig. 2d). Similar processes drive T_{Ant} via Southern Ocean sea ice, ocean heat loss and the ice-albedo feedback[24] (Fig. 2c), though the magnitudes are smaller and the timescale is longer as Antarctica responds primarily to the slow OHC mode rather than the fast DO mode.

Climate system variables marked with green triangles in Fig. 2b respond primarily to the DO mode and therefore strongly (anti-)correlate with Q (Extended Data Fig. 6b). These include the AMOC strength, North Atlantic sea ice extent and surface ocean heat flux, Greenland temperature and the TOA radiative flux imbalance. Those marked with purple asterisks strongly (anti-)correlate with OHC (Extended Data Fig. 6c), including Southern Ocean sea ice extent and surface heat flux and Antarctic temperature. The three climate models show similar behaviour for the North Atlantic DO mode with just minor quantitative differences in T_{GL} and the extent of sea ice. In the southern high latitudes the COSMOS model behaves differently (Methods), as sea ice extent, SST and T_{Ant} are insensitive to OHC in that model—in contrast with Antarctic ice core observations.

Dependence on climate background

DO timing characteristics (including their absence and occurrence) depend on background climate such as atmospheric CO_2[5,9], orbit[6,7] and ice volume[39,40], with observational data suggesting an organizing principle in which broadly warmer glacial climates have longer interstadial durations[17,18]. Next, we evaluate our energetics framework using a series of CCSM4 simulations under different atmospheric CO_2 levels, yet with fixed orbit and ice volume[5]. The model simulates permanent stadial (weak AMOC) and interstadial (strong AMOC) modes at low (≤170 ppm) and high glacial (≥240 ppm) CO_2, respectively, and oscillatory behaviour at intermediate CO_2 (Fig. 4). In agreement with observations[18], the duration and time fraction spent in interstadial periods increases with CO_2. Raising CO_2 increases (time-averaged) heat uptake Q in all ocean basins except for the North Atlantic, reflecting enhanced radiative forcing following the greenhouse effect (Extended Data Fig. 7). This enhanced ocean heat uptake Q_{UP} is balanced by a greater time-average

https://doi.org/10.1038/s41561-026-02070-6

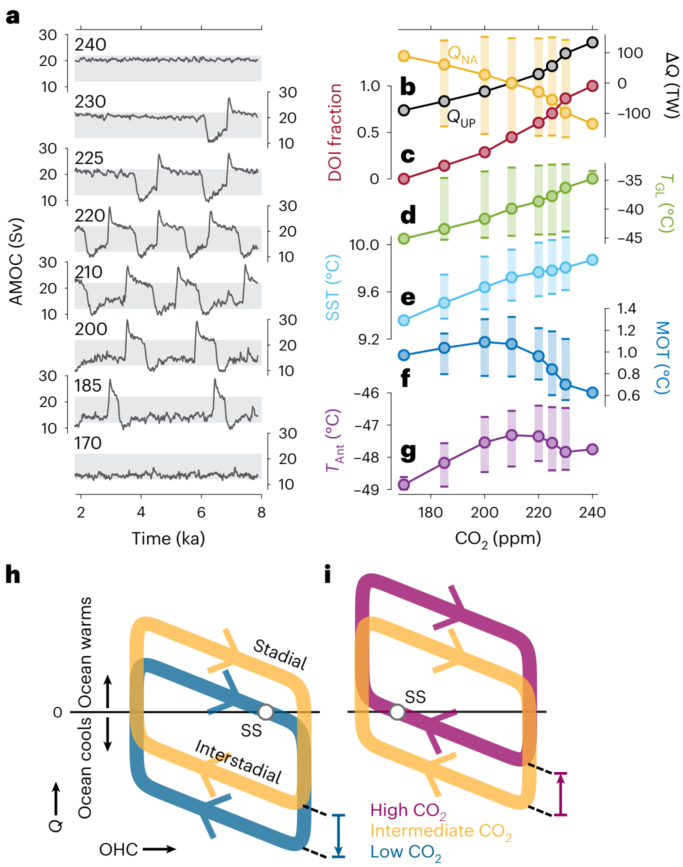

Fig. 4 | Ocean heat budget and AMOC stability as function of atmospheric CO_2. **a**, Simulated AMOC variability with CO_2 concentrations listed. **b**, Ocean surface heat flux anomaly in the North Atlantic (Q_{NA}, yellow) and in the global ocean except the North Atlantic (Q_{UP}, black) relative to the default 210 ppm CO_2 simulation. **c**, The fraction of time the system spends in the DO interstadial (DOI) mode. **d**, Greenland temperature. **e**, Global-mean SST. **f**, Global mean ocean temperature (MOT). **g**, Antarctic temperature. In panels **b**–**g**, the vertical bars denote the full range, and the round markers the long-term-average value; time-averaging is done over 5 ka and multiple DO cycles. **h**,**i**, Conceptual shifts to the Q-OHC diagram under reduced (**h**) and increased (**i**) atmospheric CO_2 levels. Steady-state climate (marked SS) is possible whenever either branch intersects the horizontal axis ($Q = 0$). Note that the pictured trajectory shifts are idealized with respect to the position of the abrupt transitions (compare Extended Data Fig. 9a).

North Atlantic heat loss Q_{NA} associated with additional time spent in the strong AMOC phase (Fig. 4b and Extended Data Fig. 7d). Whereas the imbalance between Q_{UP} and Q_{NA} drives millennial-scale OHC variations, on long timescales (multiple DO–OHC cycles), they must balance to avoid runaway change.

Whereas buoyancy and wind forcing ultimately control AMOC stability, the DO–OHC energetics suggest a helpful heuristic principle for understanding the role of CO_2. Ocean heat uptake outside the North Atlantic (Q_{UP}), which is proportional to CO_2 (Extended Data Fig. 8), balances the heat loss Q_{NA} associated with the AMOC. Given that Q_{NA} is bimodal (with distinct stadial and interstadial modes), Q_{UP} cannot be balanced by Q_{NA} at intermediate values of CO_2, resulting in oscillatory behaviour. At higher CO_2 the interstadial phase can be sustained for longer periods of time as there is more heat input into the ocean to balance interstadial AMOC heat loss. From this perspective, the DO cycle reflects an inability to balance the bimodal North Atlantic heat loss with intermediate levels of ocean heat uptake in the remainder of the ocean.

As an analogy, consider a family with an income (Q_{UP}) and savings (OHC), living in a hypothetical town with a bimodal housing cost (Q_{NA})—only cheap apartments (stadial/weak AMOC) and expensive villas (interstadial/strong AMOC), with no intermediate housing available. A low-income family living in an apartment can reach steady state between their income and expenses, and so can a high-income family in a villa. A middle-income family would oscillate between housing types, accruing savings while living in an apartment, and drawing down their savings while living in a villa. The length of time they can afford to live in expensive housing (interstadial duration) is proportional to their income.

For another perspective on AMOC stability, we consider the DO trajectory in (OHC,Q)-space (Fig. 1b). For oscillatory AMOC regimes (intermediate CO_2 levels), the 'slow' diagonal branches do not intersect the $Q = 0$ axis that corresponds to a steady-state (non-oscillatory) regime (Fig. 1b and Fig. 4h, yellow trajectory). Raising CO_2 shifts the trajectory towards more positive Q (that is, higher Q at given OHC due to added greenhouse radiative forcing; Extended Data Fig. 9). Initially, this puts the interstadial branch closer to $Q = 0$, thereby reducing the rate of interstadial heat loss and extending the interstadial duration. Further increasing CO_2 causes the interstadial branch to cross the $Q = 0$ axis, allowing a (perpetual) steady-state interstadial phase (Fig. 4i, lower branch of purple trajectory). Oppositely, lowering CO_2 shifts the trajectory towards more negative Q, eventually stabilizing a (perpetual) steady-state stadial phase (Fig. 4h, upper branch of blue trajectory).

The ocean heat valve

The three models we evaluate do not simulate the strong SST dipole between the North and South Atlantic that is central to the (thermal) bipolar seesaw concept. Rather, South Atlantic SST varies gradually and mirrors OHC (Extended Data Fig. 9b). OHC variations are synchronous in both hemispheres, with an increased northward cross-equatorial ocean heat flux during interstadials in the Atlantic and a smaller compensating (that is, southward) one in the Indo-Pacific basin[41] (Extended Data Fig. 9c,d). Rather than an interhemispheric redistribution of heat, the ocean heat valve framework suggests that the strong AMOC phase drains heat from both hemispheres alike via internal ocean heat transport anomalies towards and into the North Atlantic (Extended Data Fig. 2).

The term 'seesaw' in the context of interhemispheric climate change was first used by Thomas Crowley[21] and later adopted by Wally Broecker who added 'bipolar' to emphasize hypothesized changes in deep convection in those regions[42]. While an apt metaphor for the Atlantic SST dipole described by Crowley, it is not an accurate model for the teleconnection pattern it has since come to represent—a pattern that is planetary rather than bipolar, and involves gradual OHC changes rather than an abrupt temperature dipole. Whereas we do not seek to replace or discourage the use of historical seesaw terminology, we suggest that the 'ocean heat valve' is a more fitting descriptor. The mathematical description of the Stocker–Johnsen thermal bipolar seesaw model applies to our framework also, yet with an updated physical interpretation (Methods).

Thus far we have considered two AMOC modes, whereas the literature identifies a third, or Heinrich stadial mode[3], associated with deposition of ice-rafted debris sourced from Hudson Strait[43], amplified cooling and extended sea ice in the North Atlantic[44] and lengthened stadial duration[18]. Whereas Heinrich stadial dynamics are poorly understood, their energetics follow the DO–OHC framework with Antarctic and mean ocean warming[27] and positive TOA energy flux[45]. It is notable that this Heinrich mode is seen during all glacial terminations[46]; prolonged AMOC suppression during these periods is probably critical in increasing the planetary heat inventory (principle 2) above the threshold needed for deglaciation[23,28,47].

Interpreting the role of the AMOC in current oceanic heat uptake is challenging due to its complex impact on global ocean heat exchange, the short observational record and climate model uncertainty. The AMOC may affect the uptake efficiency of anthropogenic heat via the depth of heat sequestration in the North Atlantic[48] or its influence on the global thermocline depth and upper ocean stratification[49,50]. In parallel, future AMOC weakening could further increase OHC via reduced deep convection[35,51,52]. In this context, the glacial DO–OHC oscillation provides a valuable palaeo constraint on the effect of AMOC variability on OHC in the absence of strong radiative forcing—a scenario simpler than the modern case that has both acting in parallel. Our work establishes that future AMOC weakening would exacerbate planetary warming by throttling down the ocean heat valve.

Online content

Any methods, additional references, Nature Portfolio reporting summaries, source data, extended data, supplementary information, acknowledgements, peer review information; details of author contributions and competing interests; and statements of data and code availability are available at https://doi.org/10.1038/s41561-026-02070-6.

References

1. Grootes, P. M., Stuiver, M., White, J. W. C., Johnsen, S. & Jouzel, J. Comparison of oxygen isotope records from the GISP2 and GRIP Greenland ice cores. *Nature* **366**, 552–554 (1993).
2. Lynch-Stieglitz, J. The atlantic meridional overturning circulation and abrupt climate change. *Annu. Rev. Mar. Sci.* **9**, 83–104 (2017).
3. Rahmstorf, S. Ocean circulation and climate during the past 120,000 years. *Nature* **419**, 207–214 (2002).
4. Henry, L. G. et al. North Atlantic ocean circulation and abrupt climate change during the last glaciation. *Science* **353**, 470–474 (2016).
5. Vettoretti, G., Ditlevsen, P., Jochum, M. & Rasmussen, S. O. Atmospheric CO_2 control of spontaneous millennial-scale ice age climate oscillations. *Nat. Geosci.* **15**, 300–306 (2022).
6. Kuniyoshi, Y., Abe-Ouchi, A., Sherriff-Tadano, S., Chan, W.-L. & Saito, F. Effect of climatic precession on Dansgaard–Oeschger-like oscillations. *Geophys. Res. Lett.* **49**, e2021GL095695 (2022).
7. Zhang, X. et al. Direct astronomical influence on abrupt climate variability. *Nat. Geosci.* **14**, 819–826 (2021).
8. Klockmann, M., Mikolajewicz, U., Kleppin, H. & Marotzke, J. Coupling of the subpolar gyre and the overturning circulation during abrupt glacial climate transitions. *Geophys. Res. Lett.* **47**, e2020GL090361 (2020).
9. Malmierca-Vallet, I. et al. The impact of CO_2 and climate state on whether Dansgaard–Oeschger type oscillations occur in climate models. *Geophys. Res. Lett.* **51**, e2024GL110068 (2024).
10. Brown, N. & Galbraith, E. D. Hosed vs. unhosed: interruptions of the Atlantic Meridional Overturning Circulation in a global coupled model, with and without freshwater forcing. *Clim. Past* **12**, 1663–1679 (2016).
11. Peltier, W. R. & Vettoretti, G. Dansgaard–Oeschger oscillations predicted in a comprehensive model of glacial climate: a 'kicked' salt oscillator in the Atlantic. *Geophys. Res. Lett.* **41**, 2014GL061413 (2014).
12. Li, C. & Born, A. Coupled atmosphere-ice-ocean dynamics in Dansgaard–Oeschger events. *Quat. Sci. Rev.* **203**, 1–20 (2019).
13. Welander, P. A simple heat-salt oscillator. *Dyn. Atmos. Oceans* **6**, 233–242 (1982).
14. Ganopolski, A. & Rahmstorf, S. Rapid changes of glacial climate simulated in a coupled climate model. *Nature* **409**, 153–158 (2001).
15. Dokken, T. M., Nisancioglu, K. H., Li, C., Battisti, D. S. & Kissel, C. Dansgaard–Oeschger cycles: interactions between ocean and sea ice intrinsic to the Nordic seas. *Paleoceanography* **28**, 491–502 (2013).
16. Winton, M. The effect of cold climate upon North Atlantic deep water formation in a simple ocean–atmosphere model. *J. Clim.* **10**, 37–51 (1997).
17. Nadeau, L.-P., Jansen, M. F. & Gregorio, S. A simple model for global temperature control on Dansgaard–Oeschger oscillations. *J. Clim.* **38**, 3169–3184 (2025).
18. Buizert, C. & Schmittner, A. Southern Ocean control of glacial AMOC stability and Dansgaard-Oeschger interstadial duration. *Paleoceanography* **30**, 2015PA002795 (2015).
19. Blunier, T. & Brook, E. J. Timing of millennial-scale climate change in Antarctica and Greenland during the last glacial period. *Science* **291**, 109–112 (2001).
20. WAIS-Divide-Project-Members Precise interpolar phasing of abrupt climate change during the last ice age. *Nature* **520**, 661–665 (2015).
21. Crowley, T. J. North Atlantic deep water cools the southern hemisphere. *Paleoceanography* **7**, 489–497 (1992).
22. Stocker, T. F. & Johnsen, S. J. A minimum thermodynamic model for the bipolar seesaw. *Paleoceanography* **18**, 1087 (2003).
23. Galbraith, E. D., Merlis, T. M. & Palter, J. B. Destabilization of glacial climate by the radiative impact of Atlantic Meridional Overturning Circulation disruptions. *Geophys. Res. Lett*. https://doi.org/10.1002/2016gl069846 (2016).
24. Pedro, J. B. et al. Beyond the bipolar seesaw: toward a process understanding of interhemispheric coupling. *Quat. Sci. Rev.* **192**, 27–46 (2018).
25. Kageyama, M., Paul, A., Roche, D. M. & Van Meerbeeck, C. J. Modelling glacial climatic millennial-scale variability related to changes in the Atlantic meridional overturning circulation: a review. *Quat. Sci. Rev.* **29**, 2931–2956 (2010).
26. Shackleton, S. et al. Evolution of mean ocean temperature in Marine Isotope Stage 4. *Clim. Past* **17**, 2273–2289 (2021).
27. Bereiter, B., Shackleton, S., Baggenstos, D., Kawamura, K. & Severinghaus, J. Mean global ocean temperatures during the last glacial transition. *Nature* **553**, 39 (2018).
28. Baggenstos, D. et al. Earth's radiative imbalance from the Last Glacial Maximum to the present. *Proc. Natl. Acad. Sci. USA*. https://doi.org/10.1073/pnas.1905447116 (2019).
29. Gildor, H. & Tziperman, E. Sea-ice switches and abrupt climate change. *Philos. Trans. R. Soc. London. Ser. A* **361**, 1935–1944 (2003).
30. Weldeab, S., Friedrich, T., Timmermann, A. & Schneider, R. R. Strong middepth warming and weak radiocarbon imprints in the equatorial Atlantic during Heinrich 1 and Younger Dryas. *Paleoceanography* https://doi.org/10.1002/2016pa002957 (2016).
31. Marcott, S. A. et al. Ice-shelf collapse from subsurface warming as a trigger for Heinrich events. *Proc. Natl. Acad. Sci. USA* **108**, 13415–13419 (2011).
32. Toucanne, S. et al. Synchronous bipolar retreat of mid-latitude ice masses during Heinrich Stadials. *Nat. Geosci.* https://doi.org/10.1038/s41561-025-01887-x (2026).
33. Ganachaud, A. & Wunsch, C. Improved estimates of global ocean circulation, heat transport and mixing from hydrographic data. *Nature* **408**, 453–457 (2000).
34. Holmes, R. M. et al. Atlantic ocean heat transport enabled by Indo-Pacific heat uptake and mixing. *Geophys. Res. Lett.* **46**, 13939–13949 (2019).
35. Caesar, L., Rahmstorf, S. & Feulner, G. On the relationship between Atlantic meridional overturning circulation slowdown and global surface warming. *Environ. Res. Lett.* **15**, 024003 (2020).
36. Shackleton, N. J., Hall, M. A. & Vincent, E. Phase relationships between millennial-scale events 64,000–24,000 years ago. *Paleoceanography* **15**, 565–569 (2000).
37. Cvijanovic, I. & Chiang, J. C. H. Global energy budget changes to high latitude North Atlantic cooling and the tropical ITCZ response. *Clim. Dyn.* **40**, 1435–1452 (2013).

38. Schneider, T., Bischoff, T. & Haug, G. H. Migrations and dynamics of the intertropical convergence zone. *Nature* **513**, 45–53 (2014).
39. Zhang, X., Lohmann, G., Knorr, G. & Purcell, C. Abrupt glacial climate shifts controlled by ice sheet changes. *Nature* **512**, 290–294 (2014).
40. Sherriff-Tadano, S., Abe-Ouchi, A., Oka, A., Mitsui, T. & Saito, F. Does a difference in ice sheets between Marine Isotope Stages 3 and 5a affect the duration of stadials? Implications from hosing experiments. *Clim. Past* **17**, 1919–1936 (2021).
41. Sun, S., Thompson, A. F., Xie, S.-P. & Long, S.-M. Indo-Pacific warming induced by a weakening of the Atlantic Meridional Overturning Circulation. *J. Clim.* **35**, 815–832 (2022).
42. Broecker, W. S. Paleocean circulation during the last deglaciation: a bipolar seesaw?. *Paleoceanography* **13**, 119–121 (1998).
43. Hemming, S. R. Heinrich events: massive late Pleistocene detritus layers of the North Atlantic and their global climate imprint. *Rev. Geophys*. https://doi.org/10.1029/2003rg000128 (2004).
44. Pedro, J. B. et al. Dansgaard–Oeschger and Heinrich event temperature anomalies in the North Atlantic set by sea ice, frontal position and thermocline structure. *Quat. Sci. Rev.* **289**, 107599 (2022).
45. Shackleton, S., Seltzer, A., Baggenstos, D. & Lisiecki, L. E. Benthic $\delta^{18}O$ records Earth's energy imbalance. *Nat. Geosci.* **16**, 797–802 (2023).
46. Cheng, H. et al. Ice age terminations. *Science* **326**, 248–252 (2009).
47. Grimmer, M. et al. AMOC modulates ocean heat content during deglaciations. *Geophys. Res. Lett.* **52**, e2024GL114415 (2025).
48. Kostov, Y., Armour, K. C. & Marshall, J. Impact of the Atlantic meridional overturning circulation on ocean heat storage and transient climate change. *Geophys. Res. Lett.* **41**, 2108–2116 (2014).
49. Newsom, E., Zanna, L. & Gregory, J. Background pycnocline depth constrains future ocean heat uptake efficiency. *Geophys. Res. Lett.* **50**, e2023GL105673 (2023).
50. Vogt, L., Sallée, J. B. & de Lavergne, C. Stratification and overturning circulation are intertwined controls on ocean heat uptake efficiency in climate models. *Ocean Sci.* **21**, 1081–1103 (2025).
51. Ventrucci, C., Fabiano, F., Mehling, O., Bellomo, K. & Davini, P. AMOC weakening shapes ocean heat storage patterns under strong idealized warming. *Geophys. Res. Lett.* **53**, e2025GL120405 (2026).
52. Winton, M. et al. Has coarse ocean resolution biased simulations of transient climate sensitivity?. *Geophys. Res. Lett.* **41**, 8522–8529 (2014).

[1]College of Earth, Ocean and Atmospheric Sciences, Oregon State University, Corvallis, OR, USA. [2]Atmosphere and Ocean Research Institute, The University of Tokyo, Kashiwa, Japan. [3]Physics of Ice, Climate and Earth, Niels Bohr Institute, University of Copenhagen, Copenhagen, Denmark. [4]British Antarctic Survey, Cambridge, UK. [5]Institute of Global Environmental Change, Xi'an Jiaotong University, Xi'an, China. [6]Woods Hole Oceanographic Institution, Woods Hole, MA, USA. [7]Australian Antarctic Division, Kingston, Tasmania, Australia. [8]Australian Antarctic Program Partnership, Institute for Marine and Antarctic Studies, University of Tasmania, Hobart, Tasmania, Australia. [9]Institut de Ciència i Tecnologia Ambientals, Universitat Autònoma de Barcelona, Barcelona, Spain. [10]ICREA, Barcelona, Spain. [11]Department of Earth and Planetary Science, McGill University, Montreal, Quebec, Canada. [12]Climate and Environmental Physics and Oeschger Center for Climate Change Research, University of Bern, Bern, Switzerland. ✉e-mail: christo.buizert@oregonstate.edu

 https://doi.org/10.1038/s41561-026-02070-6

Methods

Climate models

The Community Climate System Model version 4 (CCSM4) is part of the National Center for Atmospheric Research (NCAR) Community Earth System Model (CESM1) family. The model features an approximate 3° × 3° resolution in both the atmosphere and ocean[53]. Its atmospheric component (CAM4) comprises 26 vertical levels, extending from Earth's surface to the lower stratosphere. Whereas the model includes sea ice and land surface components, it excludes ocean biogeochemistry. The land surface incorporates a simplified carbon–nitrogen cycle. CCSM4 has been widely utilized in previous Coupled Model Intercomparison Projects (CMIP5) and has demonstrated success in reproducing Dansgaard–Oeschger (D–O)-like behaviour under glacial boundary conditions[5,11]. For palaeoclimate simulations, the model employs fixed boundary conditions, including Last Glacial Maximum ice sheets, orbital insolation and prescribed atmospheric greenhouse gas concentrations. The Atlantic Meridional Overturning Circulation (AMOC) variability in modern CCSM4 simulations has been extensively documented, both for the standard resolution (~1° × 1° in ocean and atmosphere[54]); and the lower-resolution version (3° × 3°, ref. 53). The low-resolution model reasonably simulates the modern mean AMOC strength at 15 Sv. In this study, the CCSM4 configuration differs from the original model in its treatment of tidal mixing parameterizations, which are used to estimate ocean diapycnal diffusivity. Specifically, a fixed background diffusivity profile, varying only vertically, was applied in this higher-resolution simulation (ref. 5). Additionally, tidal mixing and overflow parameterizations were disabled. These modifications were implemented due to the limited constraints on ice age turbulent kinetic energy dissipation from tide–bathymetry interactions and ice age bathymetric overflows. In this study, we use experiments from ref. 5, which are characterized by millennial-scale spontaneous self-oscillatory AMOC under constant orbital configuration, ice volume and atmospheric CO_2 level—we use a simulation with constant 210 ppm CO_2 for most analyses, with the exception of Fig. 4, where we use eight simulations with constant CO_2 ranging from 170 to 240 ppm.

Besides the oceanic global teleconnection mode that is the topic of this work, the CCSM4 model also shows a clear superimposed atmospheric teleconnection mode that couples the climate of both hemispheres[55]. As in observations[56], this simulated atmospheric teleconnection is in phase with the DO mode[55]. Its operation is clearly visible in the CCSM4 OHC-T_{Ant} and OHC-SIE_{SO} scatter plots (Extended Data Fig. 6c) that have two clearly separated branches.

The Model for Interdisciplinary Research on Climate (MIROC) is a fully coupled atmosphere–ocean general circulation model (AOGCM) developed in Japan, and the version MIROC4m was used for this study. The atmospheric model including the land surface component MATSIRO was used at T42 resolution (~2.8°), with 20 vertical layers. The ocean model COCO, including sea-ice dynamics formulated using viscous–elastic– plastic rheology, has a horizontal resolution of 1.4° to 0.56° in the tropics, with 43 uneven vertical layers. The model has already been used to investigate a range of palaeoclimate phenomena, especially millennial-scale abrupt glacial climate changes such as DO cycles and deglacial climates[6,40,57,58]. In this study, we use the experiment from ref. 6 referred to as P270, which is characterized by millennial-scale spontaneous self-oscillatory AMOC under constant orbital configuration, ice volume and atmospheric CO_2 level (220 ppm).

For the calculation of the MIROC wintertime (DJF) mixed-layer depth (MLD), we used model output generated on a new supercomputer (Earth Simulator 4 at the Japan Agency for Marine-Earth Science and Technology), employing the same climate model version (MIROC4m) and identical boundary conditions. This approach was necessary because, unfortunately, due to data storage limitations the simulated seasonal MLD was not saved for the original experiment[6] that was conducted on the older Earth Simulator 3 supercomputer. The timing of the spontaneous AMOC variability is slightly shifted in the new simulations. However, the overall characteristics of the variability, such as the oscillation period and amplitude, remain essentially unchanged. To plot the DJF MLD (Extended Data Fig. 3b) while accounting for the timing mismatch, we derived a second-order polynomial fit to the AMOC–MLD relationship based on the new simulations and applied it to the AMOC from the original experiment. In addition, a minimum MLD of 142 m was imposed. This approach yields a very strong correlation ($r = 0.98$) in the new simulations, indicating that it is a reliable approximation.

COSMOS is a comprehensive fully coupled atmosphere–ocean general circulation model (AOGCM). The atmospheric model ECHAM5[59], complemented by the land surface component JSBACH[60], was used at T31 resolution (~3.75°), with 19 vertical layers. The ocean model MPI-OM[61], including sea-ice dynamics formulated using viscous–plastic rheology[62], has a resolution of GR30 (3° × 1.8°) in the horizontal, with 40 uneven vertical layers. The model has already been used to investigate a range of palaeoclimate phenomena, especially millennial-scale abrupt glacial climate changes such as DO cycles[7,63]. In this study, we use the experiment from ref. 7 (E40ka_34kaOrb), which is characterized by millennial-scale spontaneous self-oscillatory AMOC under constant orbital configuration, ice volume and atmospheric CO_2 level (195 ppm). The COSMOS model fails to simulate realistic millennial-scale temperature variations in Antarctica (Extended Data Fig. 1), which we attribute to a de-coupling between Southern Ocean SST and global MOT, and compensating north–south heat fluxes in the Atlantic and Indo-Pacific basins (Extended Data Fig. 9).

Assessment of DO and OHC modes

In the analysis we separate the DO–OHC cycle into a DO mode, defined as the interstadial (strong AMOC) state minus the stadial (weak AMOC) state, and the OHC mode, defined as the OHC maximum minus the OHC minimum (Extended Data Fig. 10). The DO mode combines data points from multiple DO cycles, from directly before and after the abrupt events to ensure that in our evaluation the selected DO interstadial and stadial periods have comparable, neutral OHC. Likewise, in identifying the OHC mode, we combine data from multiple OHC cycles; both the OHC maximum and OHC minimum periods include both intervals of weak and strong AMOC. Therefore, there is no clear imprint of the DO mode in our plots of the OHC mode (Fig. 3f and Extended Data Figs. 4f and 5f) and vice versa.

Inter-basin heat exchange

To assess inter-basin ocean heat transport, we define

$$J_X = \frac{dE_X}{dt} + Q_X \quad (1)$$

where E_X and Q_X are the heat content and integrated surface heat flux for that basin; J_X indicates the net heat gain (or loss) of basin X via inter-basin ocean heat exchange, where we ignore tidal and geothermal heating terms that are small and constant over the timescales of interest. The calculated inter-basin heat exchange for the various basins is plotted in Extended Data Fig. 2 (black arrows), both in the long-term mean (averaging over several DO–OHC cycles), and in the DO anomaly (DO interstadial minus DO stadial). The time series of the Indo-Pacific and Atlantic inter-basin exchange are shown in Extended Data Fig. 9e. Note that with equation (1), we cannot separate the Pacific and Indian ocean components in the Southern Hemisphere, and therefore we provide one value for the Indo-Pacific (indicated with the double arrow in Extended Data Fig. 2). All three models simulate net Indo-Pacific heat export (negative J), that is amplified during DO interstadials. For the Atlantic, the CCSM4 and MIROC4m models suggest net heat export, whereas the COSMOS model simulates net heat import in the long-term average; in all three models, the net anomaly during the DO interstadial is increased inter-basin heat import into the Atlantic.

Conceptual reinterpretation of the Stocker–Johnsen equations

The thermal bipolar seesaw model of Stocker and Johnsen[22] provides a simple mathematical equation for linking bipolar ice core temperature records that is remarkably successful at fitting observations; for example, Fig. 4 in ref. 64 includes a recent evaluation. Their model is described by the first-order linear differential equation

$$\frac{dT_S(t)}{dt} = \frac{1}{\tau}\left[-T_N(t) - T_S(t)\right] \tag{2}$$

with solution

$$T_S(t) = -\frac{1}{\tau}\int_0^t \left[T_N(t-s)\, e^{-s/\tau}\right] ds + T_S(0)e^{-t/\tau} \tag{3}$$

where T_S and T_N are the southern (Antarctic) and northern (Greenland) temperature anomalies, respectively, and τ is a characteristic timescale reflecting the heat reservoir. The fit to the data is optimized for $\tau \approx 1$ ka. The model is applied to time series that are unitless, normalized and high-pass filtered to remove the orbital component.

Our framework centres on the ocean heat content $E(t)$, the time derivative of which is equal to Q. Next, we add a stabilizing term $-E(t)/\tau$ that reflects the timescale τ on which the global ocean reaches a new radiative equilibrium with an applied North Atlantic heat loss or gain. The equation describing this simple model is given by

$$\frac{dE(t)}{dt} = Q(t) - \frac{E(t)}{\tau} = \frac{1}{\tau}\left[\tau Q(t) - E(t)\right] \tag{4}$$

with solution

$$E(t) = \int_0^t \left[Q(t-s)\, e^{-s/\tau}\right] ds + E(0)e^{-t/\tau} \tag{5}$$

In our third principle we established that $T_S(t) \propto E(t)$ and $T_N(t) \propto -Q(t)$. Therefore, equations (3) and (5) are completely equivalent when evaluated with normalized, unitless time series. We find that the mathematical formulation of the Stocker–Johnsen thermal bipolar seesaw also applies to the OHC framework advocated here—however, with a different conceptual interpretation. The timescale τ is comparable to the timescale of overturning the global ocean interior, which is on the order of the ocean volume (~1.37×10^{18} m^3) divided by the global rate of deepwater formation (~48 Sv (ref. 65)) giving 0.9 ka.

Data availability

This paper uses previously published model simulations that are available through refs. 5–7 and via Zenodo at https://doi.org/10.5281/zenodo.20801585 (ref. 66). CCSM4 simulations at variable CO_2 concentrations are further archived at https://sid.erda.dk/cgi-sid/ls.py?share_id=Fo2F7YWBmv.

Code availability

MATLAB code used for making figures is archived via GitHub at https://github.com/ChristoBuizert/ocean_heat_valve.

References

53. Shields, C. A. et al. The low-resolution CCSM4. *J. Clim.* **25**, 3993–4014 (2012).
54. Danabasoglu, G. et al. Variability of the atlantic meridional overturning circulation in CCSM4. *J. Clim.* **25**, 5153–5172 (2012).
55. Svensson, A. et al. Bipolar volcanic ice-core synchronization of the entire last glacial period. *Quat. Sci. Rev.* **375**, 109755 (2026).
56. Buizert, C. et al. Abrupt ice-age shifts in southern westerly winds and Antarctic climate forced from the north. *Nature* **563**, 681–685 (2018).
57. Kawamura, K. et al. State dependence of climatic instability over the past 720,000 years from Antarctic ice cores and climate modeling. *Sci. Adv.* **3**, e1600446 (2017).
58. Obase, T. & Abe-Ouchi, A. Abrupt Bølling–Allerød warming simulated under gradual forcing of the last deglaciation. *Geophys. Res. Lett.* **46**, 11397–11405 (2019).
59. Roeckner, E. et al. The atmospheric general circulation model ECHAM 5. PART I: model description. Technical Report 349 https://pure.mpg.de/rest/items/item_995269_4/component/file_995268/content (Max Planck Institute for Meteorology, 2003)
60. Brovkin, V., Raddatz, T., Reick, C. H., Claussen, M. & Gayler, V. Global biogeophysical interactions between forest and climate. *Geophys. Res. Lett.* **36**, L07405 (2009).
61. Marsland, S. J., Haak, H., Jungclaus, J. H., Latif, M. & Röske, F. The Max-Planck-Institute global ocean/sea ice model with orthogonal curvilinear coordinates. *Ocean Modell.* **5**, 91–127 (2003).
62. Hibler, W. III A dynamic thermodynamic sea ice model. *J. Phys. Oceanogr.* **9**, 815–846 (1979).
63. Zhang, X., Knorr, G., Lohmann, G. & Barker, S. Abrupt North Atlantic circulation changes in response to gradual CO_2 forcing in a glacial climate state. *Nat. Geosci.* **10**, 518–523 (2017).
64. Buizert, C. The thermal bipolar seesaw during abrupt climate change. *Encycl. Quat. Sci.* https://doi.org/10.1016/B978-0-323-99931-1.00119-7 (2025).
65. Talley, L. D. Closure of the global overturning circulation through the Indian, Pacific, and Southern oceans: schematics and transports. *Oceanography* **26**, 80–97 (2013).
66. Abe-Ouchi, A., Vettoretti, G., Zhang, X. & Kuniyoshi, Y. Planetary energy budget during abrupt glacial climate events set by Atlantic Ocean heat valve. *Zenodo* https://doi.org/10.5281/zenodo.20801585 (2026).

Author contributions

A.A.-O., G.V., X.Z. and Y.K. contributed model simulations and evaluation. C.B., S.S., S.O.R., J.B.P., E.D.G. and T.F.S. made conceptual contributions to the development of the conceptual framework. C.B. performed data analysis, created figures and drafted the manuscript. All authors edited and commented on the manuscript.

Funding

We gratefully acknowledge financial or technical support from the US National Science Foundation awards 2102944 and 2315928 (C.B.); the National Key Research and Development Program of China 2023YFF0805200 and the National Large Scientific and Technological Infrastructure 'Earth System Numerical Simulation Facility' CSTR:31134.02.EL (X.Z.); the Australian Antarctic Science project 4632 and Australian Government Department of Industry Science Energy and Resources grant ASCI000002 (J.B.P.); Canada Research Chairs Program fund number CRC-2020-00108 (E.D.G.); and the Swiss National Science Foundation grant 200492 (T.F.S.). The funders had no role in study design, data collection and analysis, decision to publish or preparation of the manuscript.

Competing interests

The authors declare no competing interests.

Additional information

Extended data is available for this paper at https://doi.org/10.1038/s41561-026-02070-6.

https://doi.org/10.1038/s41561-026-02070-6

Supplementary information The online version contains supplementary material available at https://doi.org/10.1038/s41561-026-02070-6.

Correspondence and requests for materials should be addressed to Christo Buizert.

Peer review information *Nature Geoscience* thanks Stefan Rahmstorf and the other, anonymous, reviewer(s) for their contribution to the peer review of this work. Peer reviewer reports are available.

https://doi.org/10.1038/s41561-026-02070-6

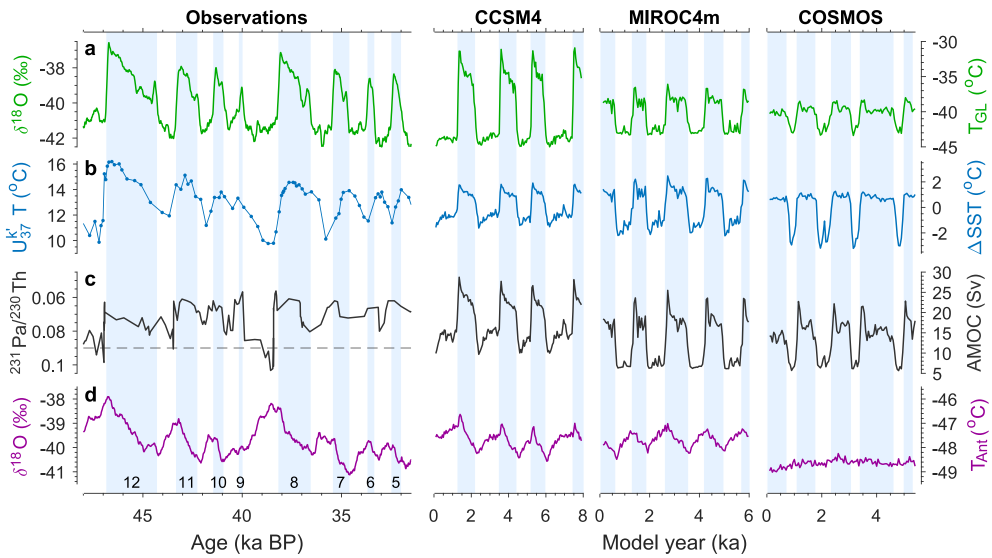

Extended Data Fig. 1 | Millennial-scale climate change of the last Ice Age in observations and climate model simulations. (**a**) Greenland Summit temperature from the ice core ^{18}O proxy[1] (left) and in simulations (right), scaled to have the same range for data and models using a sensitivity of 0.4 ‰ K^{-1}. (**b**) Iberian margin sea surface temperature (SST) from the alkenone unsaturation index $U^{k'}_{37}$ in core ODP977 (left) and in simulations (right), scaled to have the same data range. (**c**) AMOC strength from a compilation of the Bermuda rise ^{231}Pa/^{230}Th proxy[4] (left), and in simulations (right). (**d**) Antarctic temperature from the WAIS Divide ice core ^{18}O proxy[20] (left) and in simulations (right), scaled to have the same range for data and models using a sensitivity of 1 ‰ K^{-1}. Vertical blue shading indicates interstadial (strong AMOC) conditions.

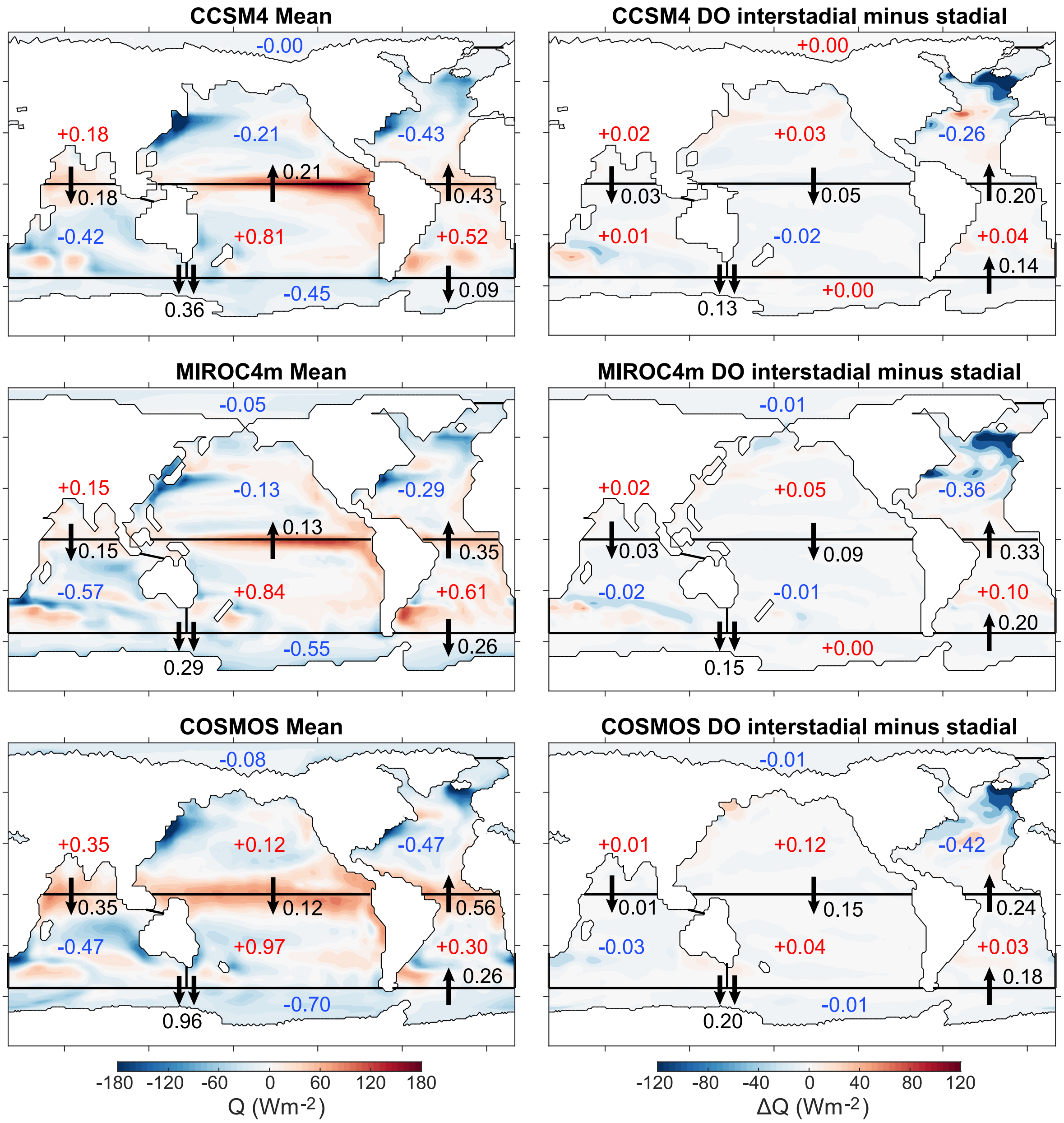

Extended Data Fig. 2 | Ocean surface heat fluxes and inter-basin transport. Simulated surface ocean heat flux (shading) in units of W m^{-2}, with positive values denoting ocean heat uptake. The left column shows the long-term mean across multiple DO-OHC cycles, whereas the right column shows the DO interstadial (strong AMOC) minus DO stadial (weak AMOC) values. Black lines demark the ocean basins as defined in this study. Red (ocean heat gain) and blue (ocean heat loss) numbers give the basin-integrated surface heat flux in units of PW (10^{15} W). Black arrows with values denote inter-basin heat exchange J (Eq. 1) in units of PW. Note that we provide one value for the Indo-Pacific heat export (double arrow south of Australia), as Eq. (1) does not allow us to calculate it separately for the Indian and Pacific Oceans due to the Indonesian throughflow.

https://doi.org/10.1038/s41561-026-02070-6

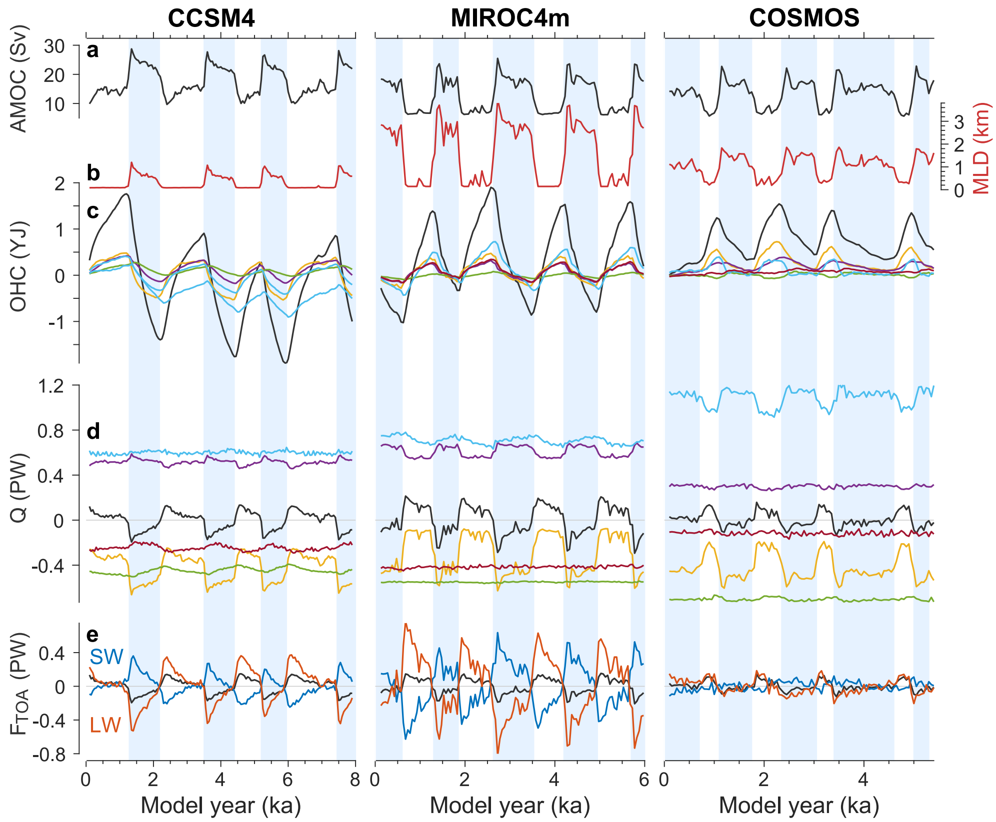

Extended Data Fig. 3 | The DO-OHC oscillation in the CCSM4 (left), MIROC4m (middle), and COSMOS (right) climate models. Time series of spontaneous DO-OHC oscillations in (**a**) AMOC strength (Sv = 10^6 m^3 s^{-1}); (**b**) North Atlantic maximum wintertime (DJF) mixed-layer depth in the simulated deep convection region of the subpolar gyre; (**c**) Ocean heat content (OHC) of different ocean basins (color coded as listed, YJ = 10^{24} J); (**d**) total ocean surface heat flux of different ocean basins (positive means ocean heat uptake, same color coding as OHC plot); (**e**) Top-of-atmosphere (TOA) total (grey), net longwave (orange), and net shortwave (blue) radiative flux anomalies (positive means planetary energy uptake). Vertical blue shading indicates interstadial (strong AMOC) conditions.

https://doi.org/10.1038/s41561-026-02070-6

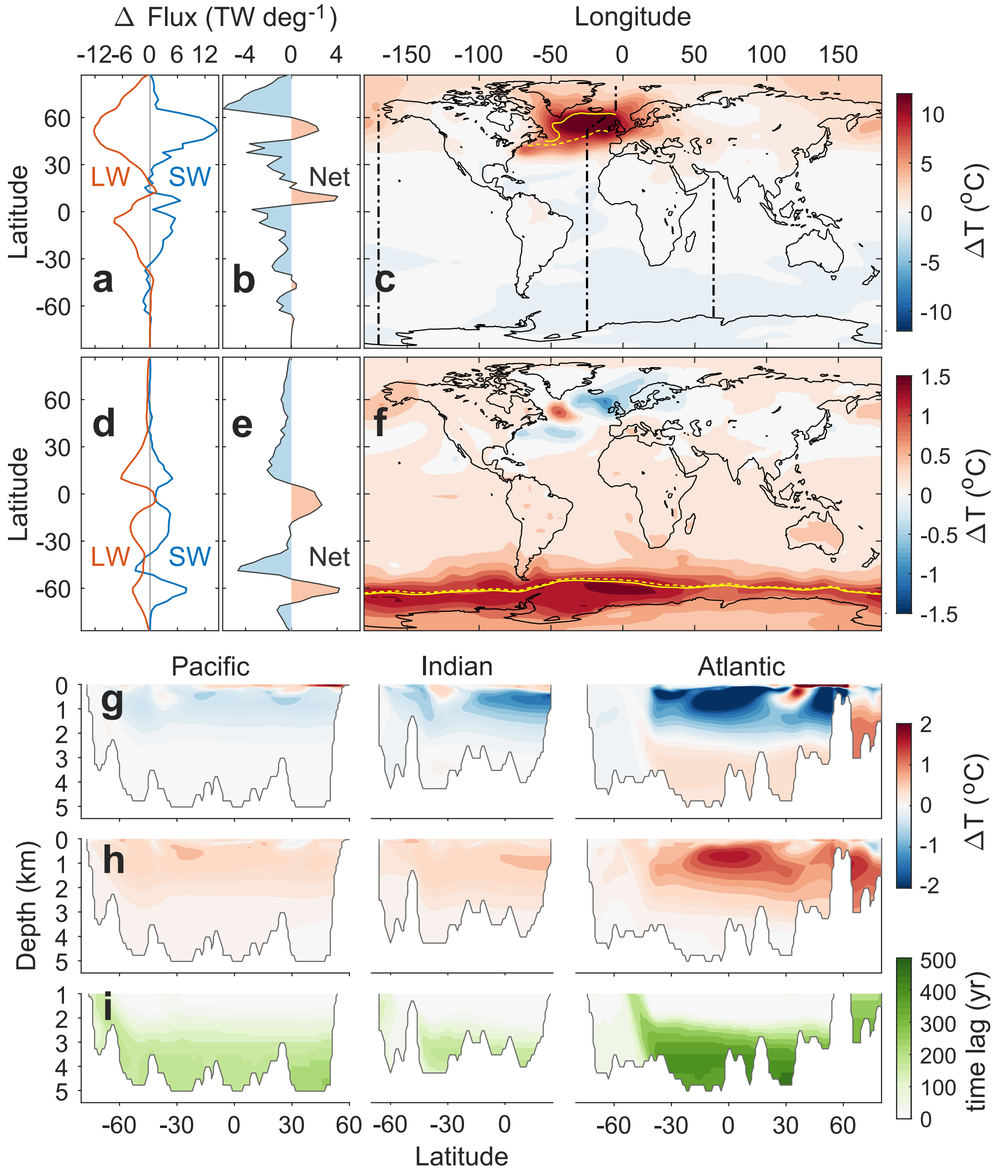

Extended Data Fig. 4 | Temperature and flux anomalies of the DO-OHC cycle in the MIROC4m model. (**a**-**c**) DO mode anomalies as interstadial minus stadial conditions (see Extended Data Fig. 10): (**a**) top-of-atmosphere (TOA) zonal-mean longwave and shortwave flux anomalies in units of TW per degree of latitude; (**b**) net TOA radiative flux anomalies; and (**c**) surface air temperature anomalies with winter sea ice extent in interstadial (yellow solid line) and stadial (yellow dashed line) conditions. Black dashed lines give the location of the basin-specific ocean transects throughout this paper. (**d**-**f**) As for panels (**a**-**c**), but for ocean heat content (OHC) maximum minus OHC minimum conditions; winter sea ice extent in OHC maximum (yellow solid line) and OHC minimum (yellow dashed line). (**g**) Ocean potential temperature anomalies along meridional transects for the DO mode (interstadial minus stadial conditions). (**h**) as panel (**e**) but for the OHC mode (OHC maximum minus OHC minimum conditions). (**i**) Time lag that maximizes the Pearson correlation coefficient between local temperature, and global-mean ocean temperature. All simulates from the MIROC4m model (Methods).

https://doi.org/10.1038/s41561-026-02070-6

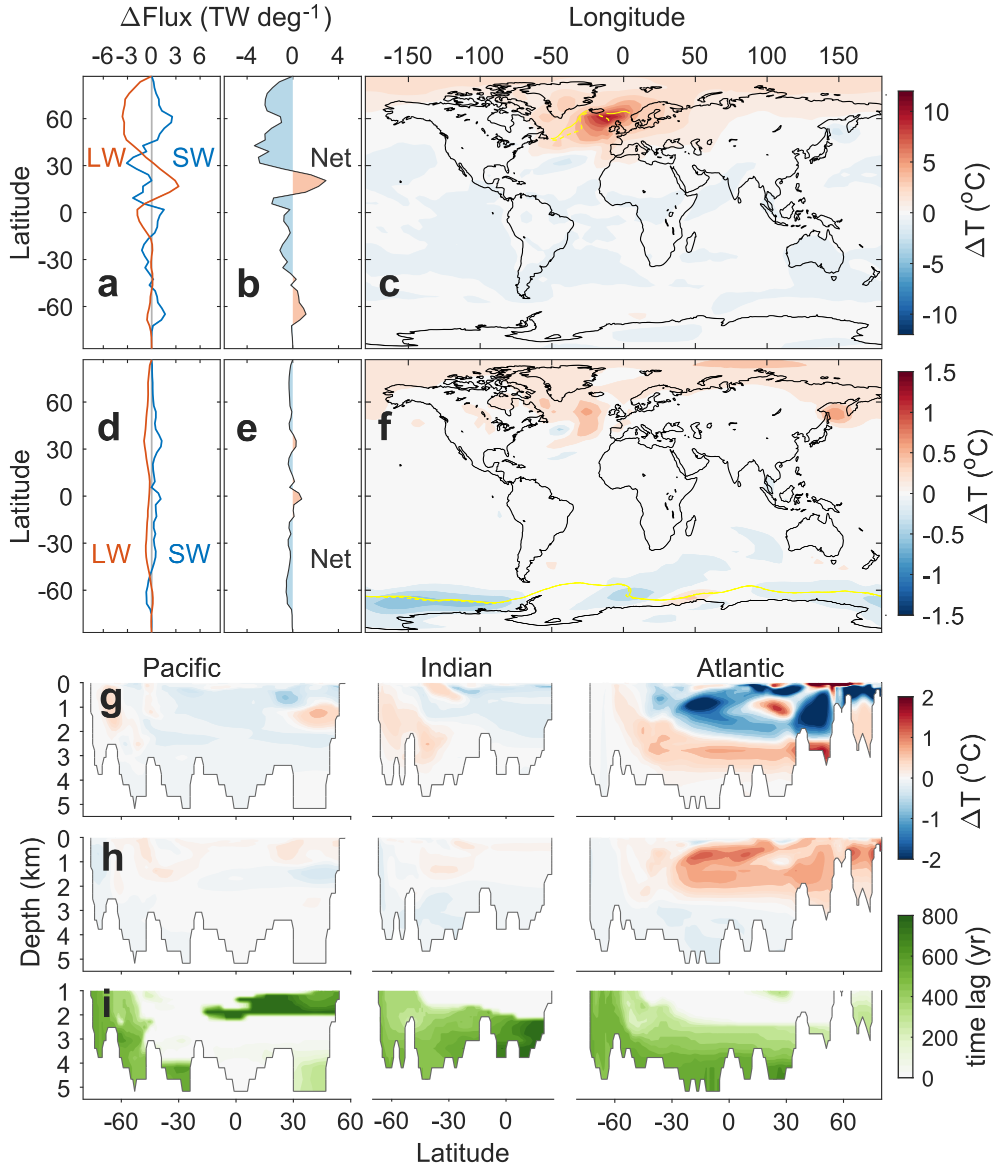

Extended Data Fig. 5 | Temperature and flux anomalies of the DO-OHC cycle in the COSMOS model. (**a-c**) DO mode anomalies as interstadial minus stadial conditions (see Extended Data Fig. 10): (**a**) top-of-atmosphere (TOA) zonal-mean longwave and shortwave flux anomalies in units of TW per degree of latitude; (**b**) net TOA radiative flux anomalies; and (**c**) surface air temperature anomalies with winter sea ice extent in interstadial (yellow solid line) and stadial (yellow dashed line) conditions. (**d-f**) As for panels (**a-c**), but for ocean heat content (OHC) maximum minus OHC minimum conditions; winter sea ice extent in OHC maximum (yellow solid line) and OHC minimum (yellow dashed line). (**g**) Ocean potential temperature anomalies along meridional transects for the DO mode (interstadial minus stadial conditions). (**h**) as panel (**e**) but for the OHC mode (OHC maximum minus OHC minimum conditions). (**i**) Time lag that maximizes the Pearson correlation coefficient between local temperature, and global-mean ocean temperature. All simulates from the COSMOS model (Methods).

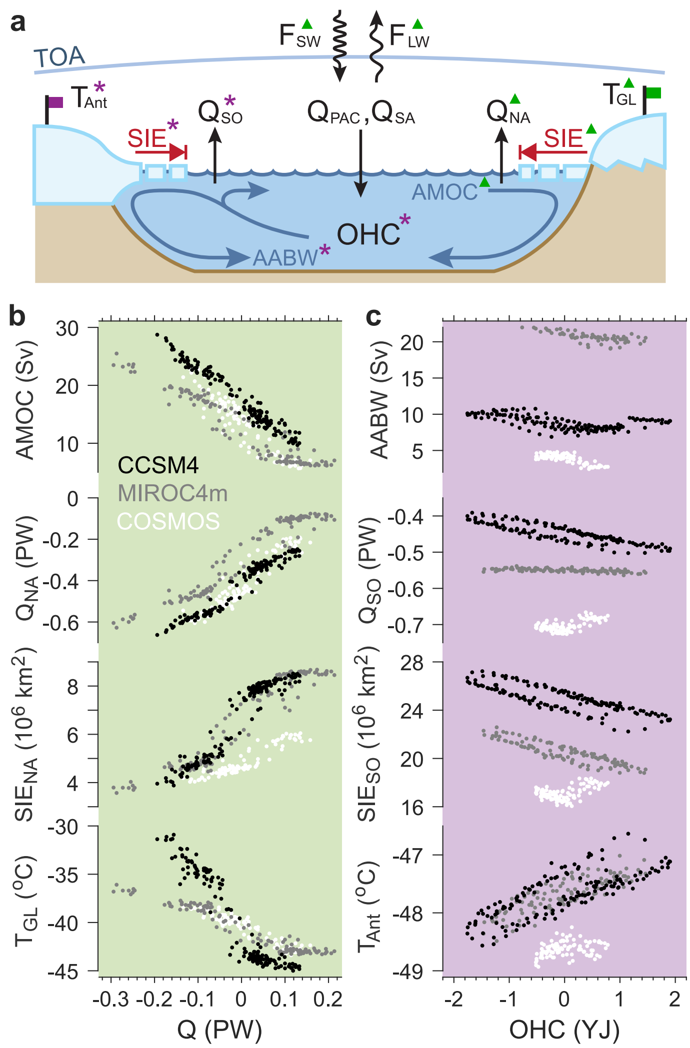

Extended Data Fig. 6 | Correlations between variables in the climate models. (**a**) Idealized ocean cross-section with variables of interest: Top of the atmosphere (TOA) net incoming shortwave (F_{SW}) and net outgoing longwave (F_{LW}); ocean surface heat fluxes in Southern (Q_{SO}), Pacific (Q_{PAC}), South Atlantic (Q_{SA}), and North Atlantic (Q_{NA}) Oceans; Sea Ice Extent (SIE) in the Southern Ocean and North Atlantic; Antarctic (T_{Ant}) and Greenland (T_{GL}) temperatures; ocean heat content (OHC); AMOC and Antarctic Bottom Water (AABW) overturning circulation. Variables marked with green triangles (anti-) correlate with Q, variables marked with purple asterisks (anti-) correlate with OHC. Arrows indicate physical direction of heat transport. (**b**) Simulated variables that (anti-) correlate with Q. From top to bottom: AMOC strength, North Atlantic surface heat flux, North Atlantic sea ice extent, and Greenland temperature. (**c**) Simulated variables that (anti-) correlate with OHC. From top to bottom: AABW strength, Southern Ocean surface heat flux, Southern Ocean sea ice extent, and Antarctic temperature. Models are color coded, with CCSM4 in black, MIROC4m in grey, and COSMOS in white.

https://doi.org/10.1038/s41561-026-02070-6

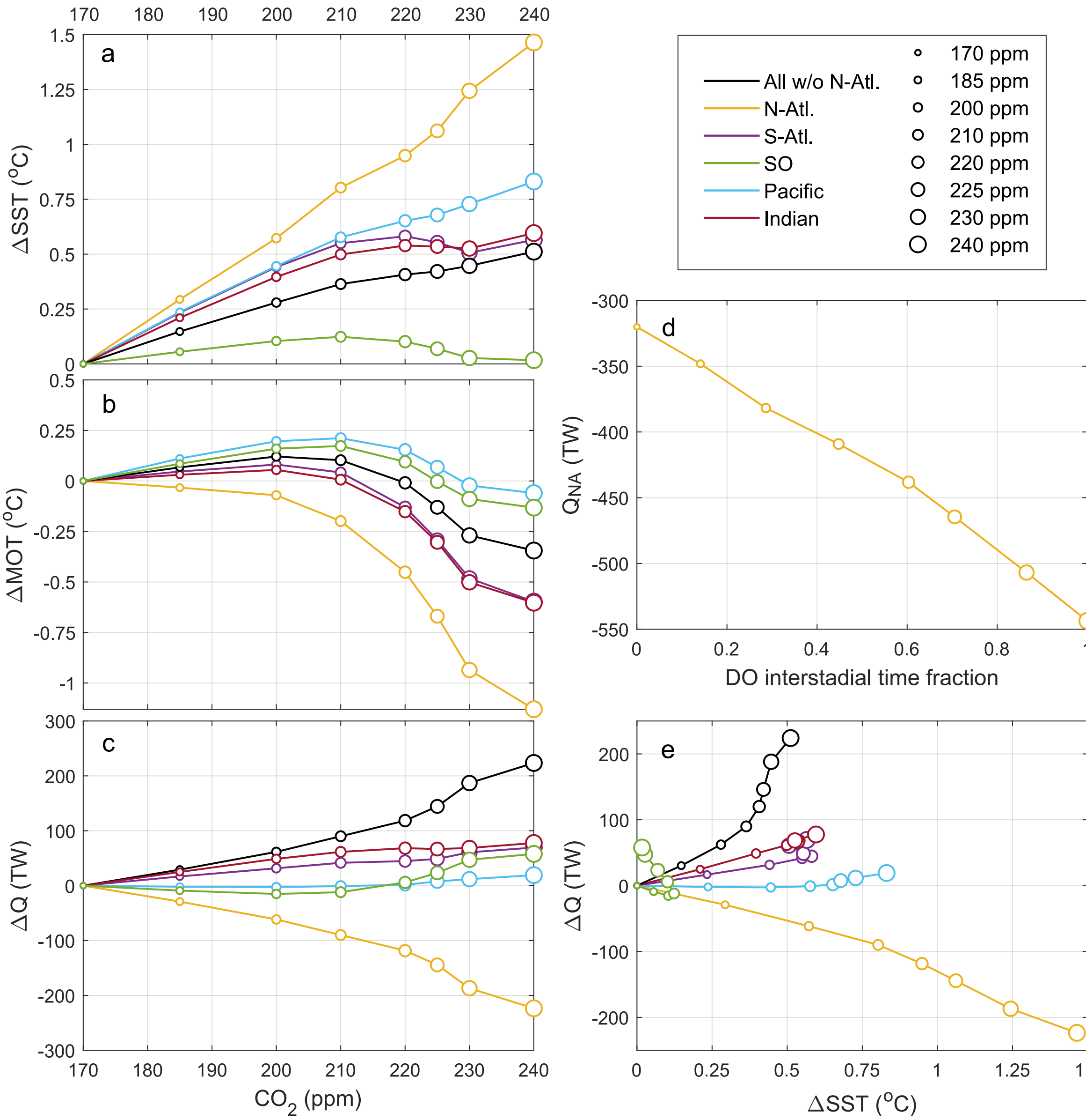

Extended Data Fig. 7 | Basin evaluation of the DO-OHC cycle long-term-average energetics as a function of background CO_2 level. (**a**) Basin long-term-averaged sea surface temperature (SST) anomaly as a function of CO_2, relative to the 170 ppm case. SST values are averaged over the last 5 ka of each simulation, and cover both stadial and interstadial conditions. Basins are color coded as per the legend. (**b**) As for (a), but for the basin-averaged mean ocean temperature (MOT). (**c**) As for (a), but for the basin-averaged surface heat flux Q. (**d**) Scatter plot of long-term average Q_{NA} vs. interstadial duration, with marker size denoting CO_2 concentration as per the legend. (**e**) Scatter plot of basin-average SST vs. basin-average Q, with the marker size reflecting the CO_2 concentration as per the legend. Values are averaged over the last 5,000 years of each simulation.

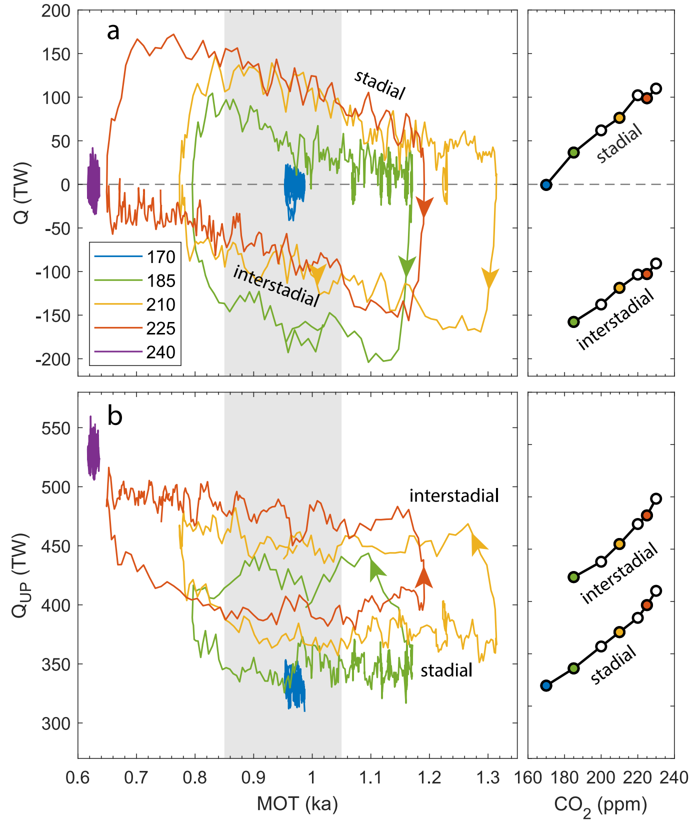

Extended Data Fig. 8 | The DO-OHC cycle as a function of background CO_2 level. **(a)** Left: the DO-OHC cycle in MOT-*Q* (mean ocean temperature-surface ocean heat flux) space for five different CO_2 concentrations as color-coded. For clarity, only a single cycle is shown at each concentration. A 30-yr running mean has been applied. Right: global surface ocean heat flux *Q* as a function of CO_2 for the stadial (upper, $Q \geq 0$) and interstadial (lower, $Q \leq 0$) branches. Values plotted are averages over a range of MOT values as denoted with the grey shaded bar in the left panel; This range is selected to be in the middle of the full range of simulated MOT values (0.55 to 1.3 °C)—note that the 240 ppm simulation falls outside of this range, and is therefore not evaluated in the right panel. (**b**) Same as panel (**a**), but for Q_{UP} instead of *Q*, with Q_{UP} reflecting the heat uptake in the global ocean excluding the North Atlantic. The heat uptake Q_{UP} balances the heat loss by the AMOC. Note that increasing CO_2 leads to enhanced heat uptake at all points along the trajectory. Note that there is a separation between the stadial (lower) and interstadial (upper) branches.

https://doi.org/10.1038/s41561-026-02070-6

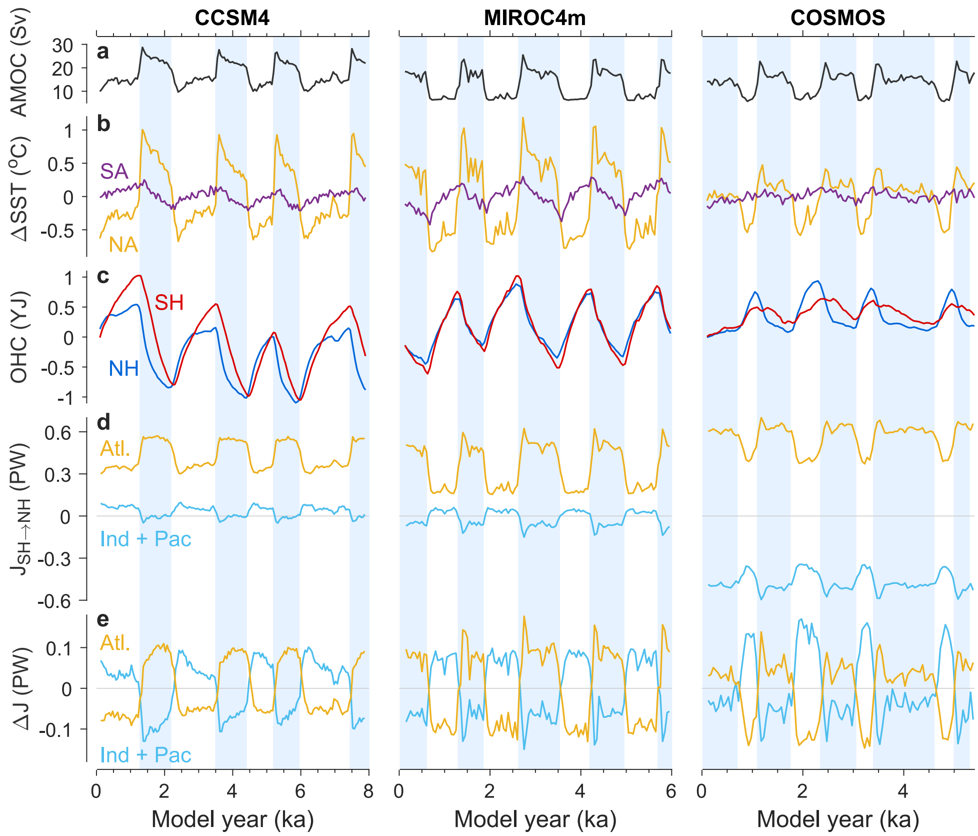

Extended Data Fig. 9 | Assessment of traditional thermal bipolar seesaw metrics and inter-basin heat exchange in the CCSM4 (left), MIROC4m (middle), and COSMOS (right) climate models. (**a**) AMOC strength (Sv = 10^6 m^3 s^{-1}). (**b**) Sea surface temperature (SST) anomalies in the North (gold) and South (purple) Atlantic. (**c**) ocean heat content (OHC) of Northern (blue) and Southern (red) hemisphere ocean basins (YJ = 10^{24} J). (**d**) Ocean cross-equatorial south-to-north heat transport in the Atlantic (gold) and Indo-Pacific (light blue) basins (PW = 10^{15} W). (**e**) Ocean heat transport anomaly into the Atlantic (gold) and Indo-Pacific (light blue) basins (positive values indicate energy added to specified basin). Vertical blue shading indicates interstadial (strong AMOC) conditions.

https://doi.org/10.1038/s41561-026-02070-6

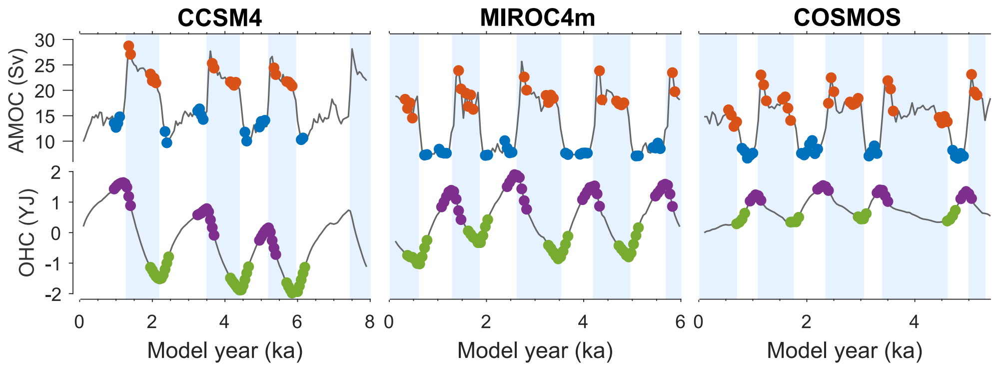

Extended Data Fig. 10 | Defining the DO and OHC modes in the CCSM4 (left), MIROC4m (middle), and COSMOS (right) climate models. Model time slices (50 year averages) used in calculations of interstadial (strong AMOC) and stadial (weak AMOC) conditions are marked with orange and blue dots, respectively; those used in calculations of OHC maximum and OHC minimum conditions are marked with purple and green dots, respectively. Vertical blue shading indicates interstadial (strong AMOC) conditions.